

# Ultrahigh Quantum Efficiency Near-Infrared-II Emission Achieved by Cr<sup>3+</sup> Clusters to Ni<sup>2+</sup> Energy Transfer

Chih-Yu Chang, Ming-Hsuan Huang, Kuan-Chun Chen, Wen-Tse Huang, Mikołaj Kamiński, Natalia Majewska, Tomasz Klimczuk, Jia-Hao Chen, Ding-Hua Cherng, Kuang-Mao Lu, Wei Kong Pang, Vanessa K. Peterson, Sebastian Mahlik,\* Grzegorz Leniec,\* and Ru-Shi Liu\*



Cite This: *Chem. Mater.* 2024, 36, 3941–3948



Read Online

ACCESS |



Metrics & More

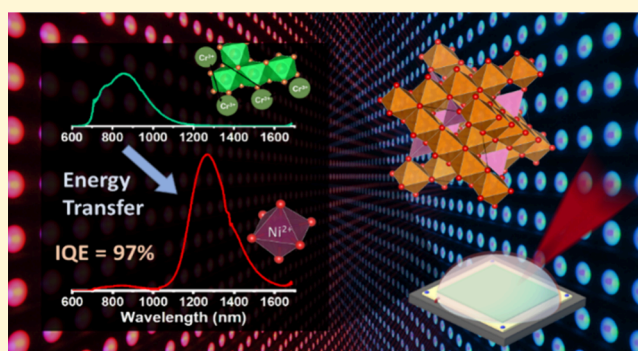


Article Recommendations



Supporting Information

**ABSTRACT:** Increasing demand for near-infrared-II (NIR-II) light sources requires improved NIR-II phosphors. We present a series of phosphors codoped with Cr<sup>3+</sup> and Ni<sup>2+</sup> that possess NIR-II emission with an unprecedented internal quantum efficiency (IQE) of 97.4%. Our study reveals an energy transfer mechanism involving clusters of Cr<sup>3+</sup> where luminescent centers are closely matched in energy and where the Ni<sup>2+</sup> emission intensity can be tuned through sintering temperature. The profound electron paramagnetic resonance (EPR) studies disclose the interaction between Cr<sup>3+</sup> clusters and Cr<sup>3+</sup>–Ni<sup>2+</sup> pairs, further proving the cause of such a high IQE and the significance of Cr<sup>3+</sup> clusters. This work provides promising pathways for the development of NIR-II light-emitting diodes with outstanding efficiency by suggesting a new energy transfer source of Cr<sup>3+</sup>.



## INTRODUCTION

The near-infrared-II (NIR-II) emission region, lying between 1000 and 1700 nm,<sup>1</sup> is favored for sensing applications due to low scattering, deep penetration, and high signal-to-background ratio, enabling sensitive chemical bond detection. The NIR-II emission region has, therefore, been widely exploited for bioimaging, biodetection, noninvasive biotreatments, and nondestructive food analysis,<sup>2–5</sup> leading to increasing demand for phosphor-converted light-emitting diodes (pc-LEDs) with NIR-II emission.<sup>6</sup>

Transition metal and lanthanoid elements, such as Cr<sup>3+</sup>, Cr<sup>4+</sup>, Mn<sup>4+</sup>, Ni<sup>2+</sup>, Eu<sup>2+</sup>, Er<sup>3+</sup>, and Yb<sup>3+</sup>, are commonly used activators for NIR emission.<sup>7–12</sup> Among these, Ni<sup>2+</sup> exhibits broadband emission in the NIR-II region, with the emission range tunable through the crystal field.<sup>13</sup> However, the typical Ni<sup>2+</sup> excitation sources such as 808/980 nm lasers and ultraviolet (UV)/near UV chips are energy-inefficient, suffering from low quantum efficiency.<sup>14,15</sup> Wang et al.<sup>16</sup> reported a series of Cr<sup>3+</sup>/Ni<sup>2+</sup> codoped NIR phosphors Zn<sub>1+y</sub>Sn<sub>y</sub>Ga<sub>2–2y</sub>O<sub>4</sub> with a Ni<sup>2+</sup> emission intensity that can be enhanced by 450 nm blue light excitation, achieved through Cr<sup>3+</sup>–Ni<sup>2+</sup> electric dipole–dipole interactions, opening a new approach for NIR-II phosphor design. Single Cr<sup>3+</sup> to Ni<sup>2+</sup> energy transfer has been reported widely, with an internal quantum efficiency (IQE) of approximately 50%,<sup>5,17–19</sup> with a higher IQE of approximately 70% reported through energy transfer from Cr<sup>3+</sup>–Cr<sup>3+</sup> ion pairs to Ni<sup>2+</sup>.<sup>20</sup> Notably, the most efficient Cr<sup>3+</sup>–Ni<sup>2+</sup> energy

transfer in the Zn<sub>1+y</sub>Sn<sub>y</sub>Ga<sub>2–2y</sub>O<sub>4</sub> phosphor series codoped with Cr<sup>3+</sup>/Ni<sup>2+</sup> was found for compositions with an intermediate spinel-type structure, found between normal and inverse spinel-type structures.<sup>16</sup> Miao et al.<sup>21</sup> reported the intermediate spinel-type structured phosphor MgGa<sub>2</sub>O<sub>4</sub>:Cr<sup>3+</sup>,Ni<sup>2+</sup> with an ultrahigh IQE of 96.5%; however, the structural properties and luminescent mechanism were not investigated. Focusing on the MgGa<sub>2</sub>O<sub>4</sub> system, Yao et al.<sup>22</sup> reported the likely existence of Cr<sup>3+</sup>–Cr<sup>3+</sup> ion pairs in the MgGa<sub>2</sub>O<sub>4</sub> intermediate spinel-type structure, and Rajendran et al.<sup>23</sup> reported the presence of Cr<sup>3+</sup> clusters in an intermediate spinel-type structured material. Therefore, our work leverages insights into the high-efficiency energy transfer from Cr<sup>3+</sup> clusters to Ni<sup>2+</sup> in the intermediate spinel MgGa<sub>2</sub>O<sub>4</sub> structure to achieve ultrahigh IQE in the NIR-II region.

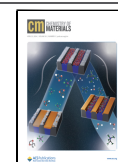
The present work investigates the energy transfer from single Cr<sup>3+</sup> ions ( $x = 0.02$ ) and Cr<sup>3+</sup> clusters ( $x = 0.06$ ) to Ni<sup>2+</sup> in the Mg<sub>1–y</sub>Ga<sub>2–x</sub>O<sub>4</sub>:xCr<sup>3+</sup>,yNi<sup>2+</sup> series with an intermediate spinel-type structure. We report detailed crystal structural analysis and luminescence properties, as well as energy transfer

Received: February 21, 2024

Revised: April 2, 2024

Accepted: April 2, 2024

Published: April 12, 2024



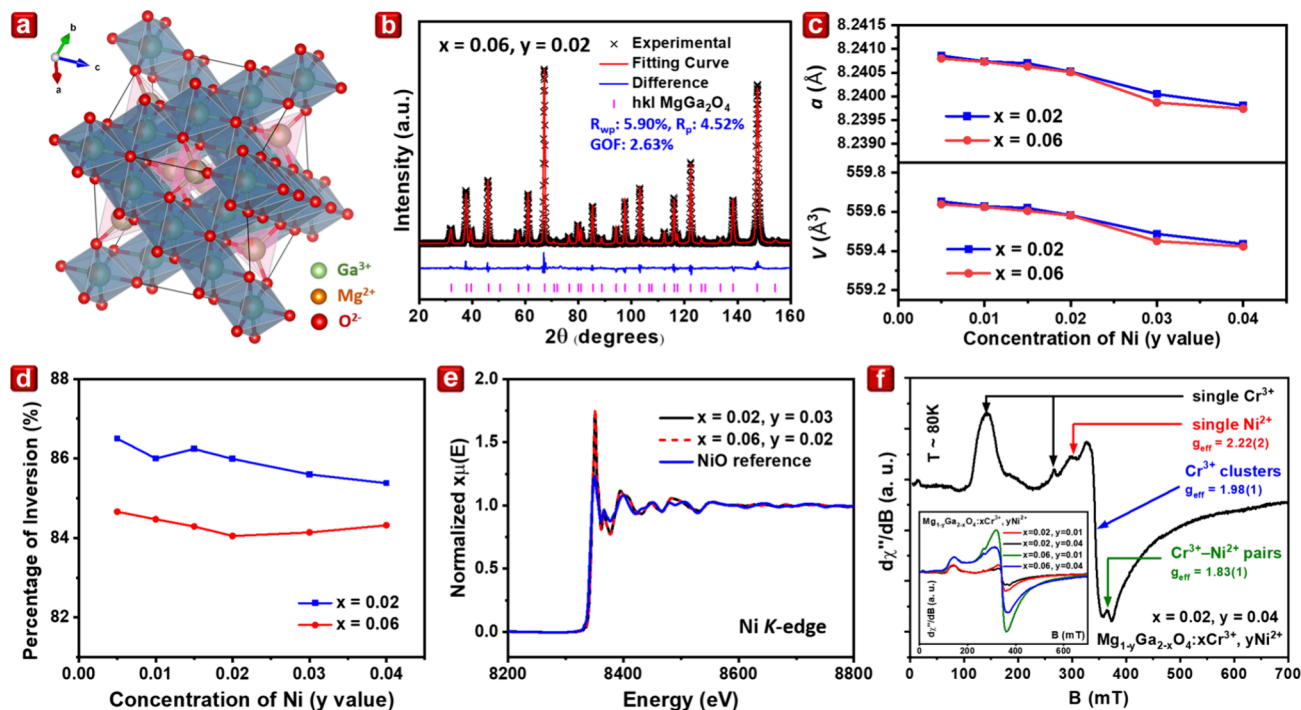


**Figure 1.** Structural characterization of  $\text{Mg}_{1-y}\text{Ga}_{2-x}\text{O}_4:x\text{Cr}^{3+},y\text{Ni}^{2+}$ . (a) Crystal structure of  $\text{MgGa}_2\text{O}_4$  (ICDD #1252694) with space group symmetry of  $Fd\bar{3}m$ . Octahedrons are colored in blue, and tetrahedrons are colored in pink; green atoms are the percentages occupied by  $\text{Ga}^{3+}$ , orange atoms are the percentages occupied by  $\text{Mg}^{2+}$ , and red atoms are those occupied by  $\text{O}^{2-}$ . (b) Rietveld refinement profile using neutron powder diffraction data (jointly refined against synchrotron X-ray powder diffraction shown in Figure S3) of  $\text{Mg}_{1-y}\text{Ga}_{2-x}\text{O}_4:x\text{Cr}^{3+},y\text{Ni}^{2+}$  at  $x = 0.06$  and  $y = 0.02$ . The figures of merit are the profile  $R_p$ , the weighted profile  $R_{wp}$ , and the goodness of fit (GOF). (c) Lattice parameter and volume and (d) calculated percentage of inversion of the  $\text{Mg}_{1-y}\text{Ga}_{2-x}\text{O}_4:x\text{Cr}^{3+},y\text{Ni}^{2+}$  series. Lines through points guide the eye, and errors are smaller than the points. (e) Ni  $K$ -edge XANES data of  $\text{Mg}_{1-y}\text{Ga}_{2-x}\text{O}_4:x\text{Cr}^{3+},y\text{Ni}^{2+}$  for  $x = 0.02, y = 0.03$  and  $x = 0.06, y = 0.02$  samples, along with the NiO reference. (f) EPR data for  $\text{Mg}_{1-y}\text{Ga}_{2-x}\text{O}_4:x\text{Cr}^{3+},y\text{Ni}^{2+}$  at 80 K, where  $g_{\text{eff}}$  is the effective value of the spectroscopic splitting ratio.

mechanisms, unveiling the importance of  $\text{Cr}^{3+}$  clusters in achieving high-efficiency NIR-II emission.

## RESULTS AND DISCUSSION

**Structural Analysis.**  $\text{MgGa}_2\text{O}_4$  has an intermediate spinel-type crystal structure with an  $Fd\bar{3}m$  space group comprising six coordinate octahedra (M1) and four coordinate tetrahedra (M2) in the ratio 2 to 1, shown in blue and pink, respectively, in Figure 1a. This structure has M1 and M2 occupied by both  $\text{Mg}^{2+}$  and  $\text{Ga}^{3+}$  and can therefore host codoped  $\text{Cr}^{3+}$  (substituting  $\text{Ga}^{3+}$ ) and  $\text{Ni}^{2+}$  (substituting  $\text{Mg}^{2+}$ , yielding luminescence<sup>24,25</sup>) to form  $\text{Mg}_{1-y}\text{Ga}_{2-x}\text{O}_4:x\text{Cr}^{3+},y\text{Ni}^{2+}$ .

$\text{Mg}_{1-y}\text{Ga}_{2-x}\text{O}_4:x\text{Cr}^{3+},y\text{Ni}^{2+}$  with  $x = 0.02, y = 0.005\text{--}0.04$  and  $x = 0.06, y = 0.005\text{--}0.04$  were characterized using laboratory powder X-ray diffraction (XRD) shown in Figure S1. The samples show high crystallinity, and all peaks could be indexed to the  $\text{MgGa}_2\text{O}_4$  structure (ICDD #1252694), indicating phase purity. Rietveld refinement of this structure using synchrotron XRD (S-XRD) (and jointly against neutron powder diffraction (NPD) data for the  $x = 0.06, y = 0.02$  composition) is shown in Figure 1b, Figures S2 and S3, and Tables S1–S4, where the figures of merit the profile  $R$ -factor ( $R_p$ ), the weighted profile  $R$ -factor ( $R_{wp}$ ), and the goodness of fit (GOF) indicate reliable results.<sup>26</sup> The refined unit cell parameter  $a$  and the unit cell volume  $V$  decrease with increasing  $\text{Ni}^{2+}$  concentration in samples with  $x = 0.02$  and  $0.06$ , as shown in Figure 1c. The decrease in  $a$  with increased  $\text{Ni}^{2+}$  is expected as a result of the smaller  $\text{Ni}^{2+}$  relative to  $\text{Mg}^{2+}$ , where  $\text{Mg}^{2+}$ (VI) has an ionic radius of 0.72 Å and  $\text{Ni}^{2+}$ (VI) of

0.69 Å, compared with  $\text{Ga}^{3+}$ (VI) of 0.62 Å.<sup>27</sup> Notably, if  $\text{Ni}^{2+}$  ions were to substitute  $\text{Ga}^{3+}$ , an increase in  $a$  is expected. The difference in  $a$  for samples with the same concentrations of  $\text{Ni}^{2+}$  but different  $\text{Cr}^{3+}$  originates from the substitution of  $\text{Ga}^{3+}$  by slightly smaller  $\text{Cr}^{3+}$ (VI) with a radius of 0.615 Å.<sup>27</sup>

Different occupancies of M1 and M2 by different cations are found, and the degree of inversion is calculated in Figure 1d, specifically determining the percentage of trivalent cations in the M2 tetrahedral site.<sup>28</sup> Both series maintained a high degree of inversion for the system of around 86 and 84% for low and high  $\text{Cr}^{3+}$  concentration samples, respectively. This reveals that the octahedral M1 site consists of around 43% of the divalent environment, where  $\text{Ni}^{2+}$  is substituted in the octahedral site, which leads to a likelihood of fewer defects.

Cr and Ga are hard to distinguish using X-ray diffraction, especially given the small Cr concentration. For this reason, we used the NPD data of the  $x = 0.06, y = 0.02$  composition sample to determine that  $\text{Cr}^{3+}$  occupies predominantly the octahedral M1 site substituting  $\text{Ga}^{3+}$ . X-ray absorption near-edge structure (XANES) measurements at the Ni  $K$ -edge for the  $x = 0.02, y = 0.03$  and  $x = 0.06, y = 0.02$  samples are shown in Figure 1e,<sup>29</sup> along with the NiO standard, revealing similar valencies of  $\text{Ni}^{2+}$ . No pre-edge is found for either sample, indicating a more symmetric, octahedral environment.<sup>30</sup> In all, we conclude that the system contains predominantly  $\text{Ni}^{2+}$  in the octahedral M1 site. The Cr XANES analysis is presented in the Supporting Information.

Electron paramagnetic resonance (EPR) studies were conducted to investigate the environment and interactions of

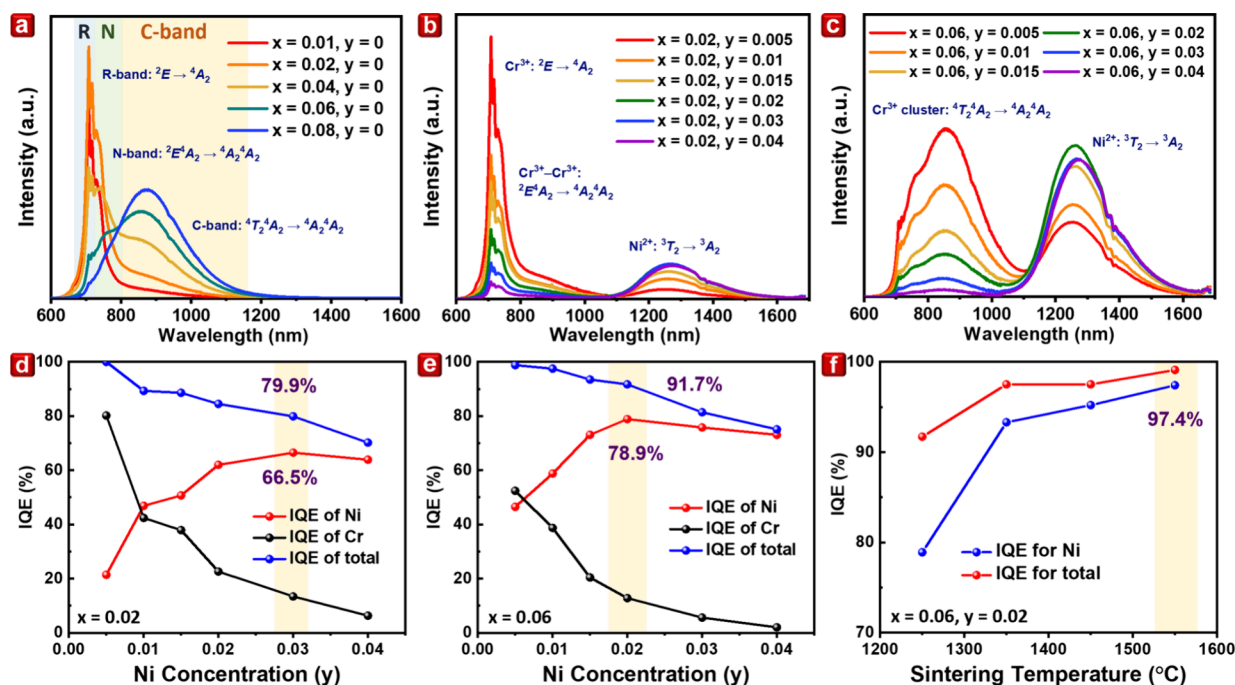


**Figure 2.** Photoluminescence properties of  $\text{Mg}_{1-y}\text{Ga}_{2-x}\text{O}_4:x\text{Cr}^{3+},y\text{Ni}^{2+}$  at room temperature. PL spectra upon excitation at 460 nm of (a)  $x = 0.01-0.08$ ,  $y = 0$ , (b)  $x = 0.02$ ,  $y = 0.005-0.04$ , and (c)  $x = 0.06$ ,  $y = 0.005-0.04$  with marked energy level transitions. Internal quantum efficiency (IQE) of (d)  $x = 0.02$ ,  $y = 0.005-0.04$ , (e)  $x = 0.06$ ,  $y = 0.005-0.04$ , and (f)  $x = 0.06$ ,  $y = 0.02$  at different sintering temperatures. Lines through the points are guides to the eye. R, N, and C band emissions are shaded in blue, green, and orange, respectively.

the paramagnetic luminescent centers.<sup>31,32</sup>  $\text{Cr}^{3+}$  ions have spin  $S = 3/2$ , and EPR spectra are recorded over the full temperature range, while  $\text{Ni}^{2+}$  ions have integer spin  $S = 1$ . Thus, the EPR signal from  $\text{Ni}^{2+}$  can be observed only at low temperatures. Figure 1f shows the EPR spectrum for a selected  $\text{Mg}_{1-y}\text{Ga}_{2-x}\text{O}_4:x\text{Cr}^{3+},y\text{Ni}^{2+}$  compound at  $T \approx 80$  K in the range of up to 700 mT. In the EPR signal, it is possible to distinguish EPR lines originating from single  $\text{Cr}^{3+}$ , single  $\text{Ni}^{2+}$ ,  $\text{Cr}^{3+}$  clusters, and  $\text{Cr}^{3+}-\text{Ni}^{2+}$  ion pairs, with the effective spectroscopic splitting ratio  $g_{\text{eff}} = 4.74/2.54$ , 2.22, 1.98, and 1.83, respectively.<sup>33-35</sup> The presence of  $\text{Cr}^{3+}$  clusters has been found and investigated by Rajendran et al.<sup>23</sup> The samples are reproduced and measured in Figure S5a and fitted using the Curie–Weiss model for single  $\text{Cr}^{3+}$  and the Bleaney–Bowers (BB) model for  $\text{Cr}^{3+}$  clusters.<sup>36,37</sup> The  $\text{Ni}^{2+}$ -doped-only samples are also synthesized and measured at 80 K in Figure S5b. The results indicate that the signal originates from a single  $\text{Ni}^{2+}$  in the octahedral site rather than  $\text{NiO}$ , where  $\text{Ni}^{2+}$  ions strongly interact with each other and where the intensity of the signal increases with increased  $\text{Ni}^{2+}$  concentration.<sup>38</sup> A decrease in the  $\text{Cr}^{3+}$  cluster signal is observed on the increasing concentration of  $\text{Ni}^{2+}$ , shown in the inset in Figure 1f and Figure S6a,b. However, this intensity decrease was not accompanied by the broadening of the signal, as shown in Figure S5a, with a change in only the concentration of  $\text{Cr}^{3+}$ . Therefore, all spin Hamiltonian (SH) parameter fittings were conducted for experimental data as shown in Figures S5c,d and S6c,d. It should be noted that the signals from single  $\text{Ni}^{2+}$  ions are in superposition with the signals from  $\text{Cr}^{3+}$  clusters. At the same time, the signal from single  $\text{Ni}^{2+}$  ions is left of the signal from  $\text{Cr}^{3+}$  clusters, and the signal from  $\text{Cr}^{3+}-\text{Ni}^{2+}$  ion pairs is right of the signal from  $\text{Cr}^{3+}$  clusters. The negative part of the signal from single  $\text{Ni}^{2+}$  ions aligns with the maximum of the positive part of the  $\text{Cr}^{3+}$  clusters, while the positive part of the

$\text{Cr}^{3+}-\text{Ni}^{2+}$  signal aligns with the maximum of the negative part of the signal from  $\text{Cr}^{3+}$  clusters. Hence, the decrease in the  $\text{Cr}^{3+}$  cluster signal does not originate from a decrease in  $\text{Cr}^{3+}$  cluster formation but from the superposition of multiple signals. This also indicates that  $\text{Ni}^{2+}$  substitutes in an environment that is different from that of  $\text{Cr}^{3+}$ . No evidence of crystal lattice defects was observed in either EPR signal ( $g_{\text{eff}} \approx 2$ ) or SH fitting parameters,<sup>39</sup> suggesting that  $\text{Ni}^{2+}$  substitutes at the octahedral  $\text{Mg}^{2+}$  site with the same ionic valency, similar ionic radii, and suitable symmetric environment, reinforcing the nominal chemical formula. Temperature-dependent magnetic susceptibility (MS) is shown in Figure S7 and confirms the EPR results.

**Photoluminescence (PL).** Basic luminescence properties of single-doped  $\text{Cr}^{3+}$  and  $\text{Ni}^{2+}$  in the  $\text{MgGa}_2\text{O}_4$  structure were reported previously by Rajendran et al.<sup>23</sup> and Suzuki et al.,<sup>40</sup> and therefore, we focus on the codoped system. The photoluminescence (PL) spectrum of single-doped  $\text{Cr}^{3+}$  samples is shown in Figure 2a as a function of the  $\text{Cr}^{3+}$  doping. The emission spectrum consists of three bands, the R-band (708 nm), the N-band (750 nm), and the C-band (850 nm), arising from the emission of single  $\text{Cr}^{3+}$ ,  $\text{Cr}^{3+}-\text{Cr}^{3+}$  pairs, and  $\text{Cr}^{3+}$  clusters, respectively.<sup>23</sup> The IQE of the samples is listed in Table S5, where an IQE > 97% up to  $x = 0.06$  is found. Based on this result, the  $x = 0.02$  and  $x = 0.06$  compositions are identified as low and high  $\text{Cr}^{3+}$  concentration groups for our  $\text{Cr}^{3+}$  to  $\text{Ni}^{2+}$  energy transfer research targeting the energy transfer mechanism from single  $\text{Cr}^{3+}$  and  $\text{Cr}^{3+}$  clusters.

The photoluminescence excitation (PLE) spectra of both series  $\text{Mg}_{1-y}\text{Ga}_{2-x}\text{O}_4:x\text{Cr}^{3+},y\text{Ni}^{2+}$ ,  $x = 0.02$ ,  $y = 0.005-0.04$  and  $x = 0.06$ ,  $y = 0.005-0.04$  are shown in Figure S8. For samples with  $x = 0.02$ , upon 708 nm observation (corresponding to the  ${}^2E \rightarrow {}^4A_2$  transition of  $\text{Cr}^{3+}$ ), the PLE

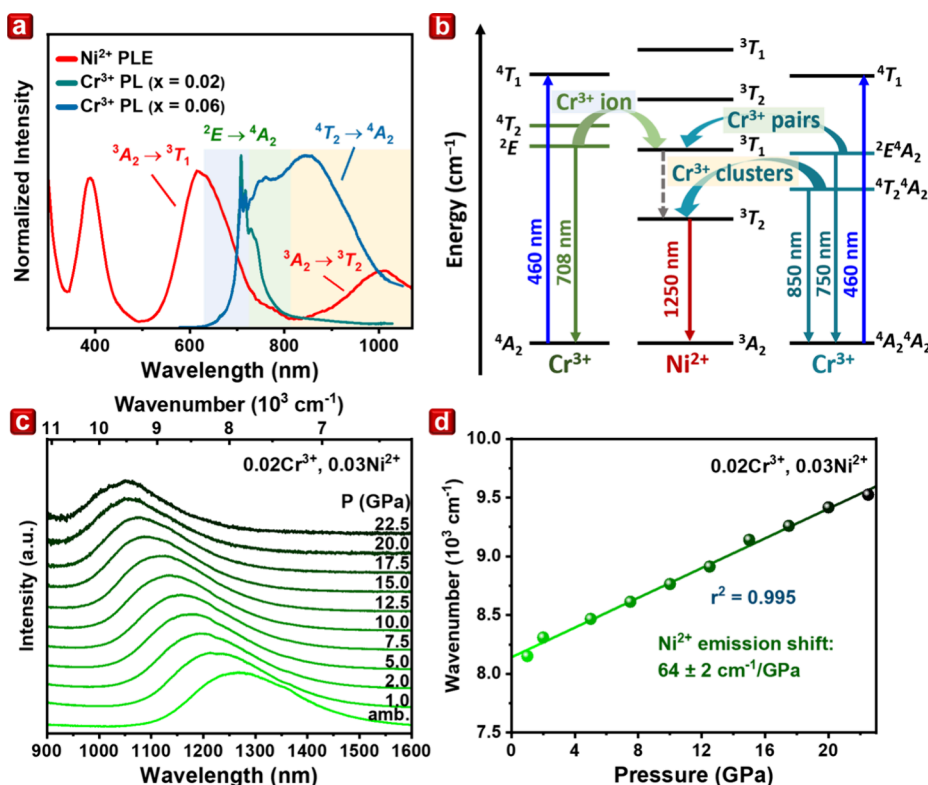


**Figure 3.** Energy transfer mechanism. (a) PL spectrum of  $\text{Mg}_{1-y}\text{Ga}_{2-x}\text{O}_4:x\text{Cr}^{3+},y\text{Ni}^{2+}$ ,  $x = 0.02$ ,  $y = 0$  and  $x = 0.06$ ,  $y = 0$  upon excitation at 420 nm, and the PLE spectrum of  $x = 0$ ,  $y = 0.005$  monitored at 1250 nm. The intensities are normalized with transitions identified. (b) Schematic of energy levels and the energy transfer mechanism for isolated  $\text{Cr}^{3+}$  and  $\text{Cr}^{3+}$  pairs and clusters. Pressure studies were performed for  $\text{Mg}_{1-y}\text{Ga}_{2-x}\text{O}_4:x\text{Cr}^{3+},y\text{Ni}^{2+}$ . (c) Pressure-dependent PL spectra for  $\text{Mg}_{1-y}\text{Ga}_{2-x}\text{O}_4:x\text{Cr}^{3+},y\text{Ni}^{2+}$ ,  $x = 0.02$ ,  $y = 0.03$  excited at 442 nm from ambient pressure to 22.5 GPa, and (d) peak energy of emission with pressure.

spectra consist of two excitation bands typical for  $\text{Cr}^{3+}$  in 6-fold octahedral coordination. The high energy band at 420 nm corresponds to the  ${}^4\text{A}_2 \rightarrow {}^4\text{T}_1$  transition. In contrast, the lower energy band at 580 nm is related to the  ${}^4\text{A}_2 \rightarrow {}^4\text{T}_2$  transition of  $\text{Cr}^{3+}$ . Upon excitation of 460 nm, the PL spectrum can be divided into two regions, short wavelength and long wavelength, arising from  $\text{Cr}^{3+}$  and  $\text{Ni}^{2+}$ , respectively, as shown in Figure 2b. The emission from  $\text{Cr}^{3+}$  consists of the R-band, corresponding to the  ${}^2\text{E} \rightarrow {}^4\text{A}_2$  transition, and the N-band, from  $\text{Cr}^{3+}$ – $\text{Cr}^{3+}$  pairs luminescence. The emission from  $\text{Ni}^{2+}$  (1100–1600 nm) corresponds to the  ${}^3\text{T}_2 \rightarrow {}^3\text{A}_2$  transition with a maximum at 1260 nm and full-width at half-maximum (fwhm) of  $\approx 210$  nm, consistent with the results of Miao et al.<sup>21</sup> The concentration of  $\text{Ni}^{2+}$  does not affect the shape of  $\text{Cr}^{3+}$  and  $\text{Ni}^{2+}$  excitation and emission spectra, but enhances the intensity of  $\text{Ni}^{2+}$  while lowering the emission of  $\text{Cr}^{3+}$  significantly. The IQE is given in Table S6 and Figure 2d. The IQE of  $\text{Cr}^{3+}$  decreased and of  $\text{Ni}^{2+}$  increased until  $y = 0.03$ , with the highest IQE = 66.5% for the low  $\text{Cr}^{3+}$  concentration series ( $x = 0.02$ ).

For the high  $\text{Cr}^{3+}$  concentration samples ( $x = 0.06$ ), the PLE is shown in Figure S8b is the same as the low  $\text{Cr}^{3+}$  concentration series, while the PL is remarkably different, as shown in Figure 2c. Though the PL spectrum is also divided into two regions, the emission from  $\text{Cr}^{3+}$  is dominated by the N-band and C-band, arising from the emission of the induced  $\text{Cr}^{3+}$ – $\text{Cr}^{3+}$  pair and  $\text{Cr}^{3+}$  clusters at high  $\text{Cr}^{3+}$  concentration, while the R-band of  $\text{Cr}^{3+}$  is still observed but much less intense by comparison. The concentration of  $\text{Ni}^{2+}$  does not change the shape of the  $\text{Cr}^{3+}$  and  $\text{Ni}^{2+}$  excitation and emission spectra. As

the concentration of  $\text{Ni}^{2+}$  increases, the emission intensity of  $\text{Ni}^{2+}$  is enhanced, whereas the emission intensity of  $\text{Cr}^{3+}$  declines, which may indicate more efficient energy transfer through  $\text{Cr}^{3+}$  clusters. The IQE values are listed in Table S7 and plotted in Figure 2e, with the IQE of  $\text{Cr}^{3+}$  decreasing and of  $\text{Ni}^{2+}$  increasing until  $y = 0.02$ , yielding a maximum IQE = 78.9% for the highest  $\text{Cr}^{3+}$  concentration ( $x = 0.06$ ), with the intensity drop for  $\text{Ni}^{2+}$  at  $y > 0.02$  suggesting concentration quenching.

The highest IQE arising from  $\text{Ni}^{2+}$  emission was obtained for  $\text{Mg}_{1-y}\text{Ga}_{2-x}\text{O}_4:x\text{Cr}^{3+},y\text{Ni}^{2+}$ ,  $x = 0.06$ ,  $y = 0.02$ , and we investigated the PL of this sample as a function of sintering temperature in the range 1250 to 1550 °C due to instrument constraints. The PL results show the emission intensity of  $\text{Cr}^{3+}$  drops, and the intensity of  $\text{Ni}^{2+}$  increases with increased sintering temperature, as shown in Figure S9, with IQE shown in Table S8 and Figure 2f resulting in an IQE from  $\text{Ni}^{2+}$  emission as high as 97.4% at the sintering temperature of 1550 °C. The cause of such phenomenon originates from the increased grain size observed in the SEM images and particle analysis, as shown in Figure S10 and Table S9, while larger grain size suppresses the formation and possibility of defects due to smaller surface area. This obtained IQE is higher than that of any reported phosphor emission in the NIR-II region to date.

**Energy Transfer Mechanism.** To understand the energy transfer mechanism in the system that gives out such high IQEs, the PLE and PL spectra of single-doped  $\text{Ni}^{2+}$  samples ( $\text{Mg}_{1-y}\text{Ga}_{2-x}\text{O}_4:x\text{Cr}^{3+},y\text{Ni}^{2+}$ ,  $x = 0$ ,  $y = 0.005$ – $0.04$ ) are shown in Figure S11. Upon observation at 1250 nm, PLE spectra

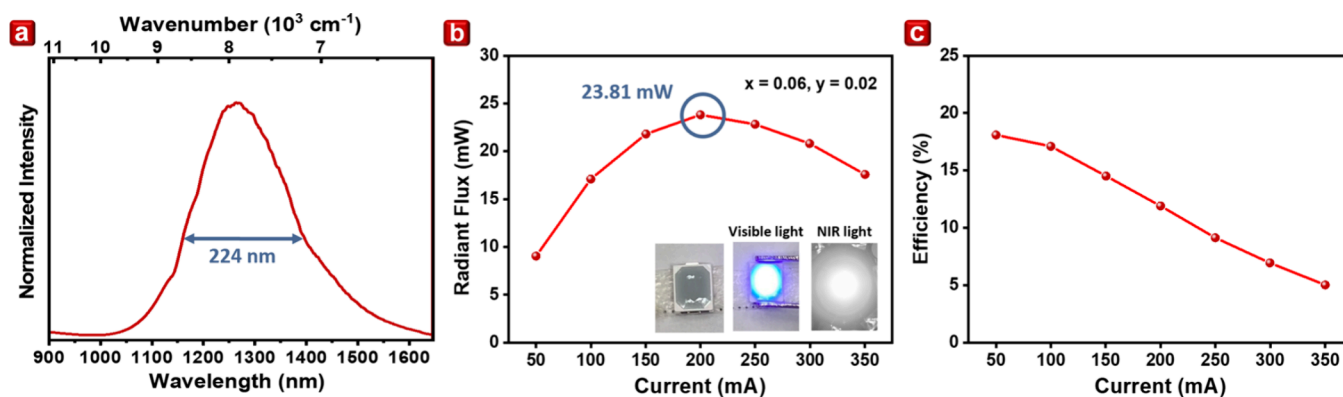


**Figure 4.** LED performance test results. (a) Emission spectrum (fwhm = full width at half-maximum = 224 nm), (b) radiant flux, and (c) efficiency of NIR pc-LEDs containing  $\text{Mg}_{1-y}\text{Ga}_{2-x}\text{O}_4:x\text{Cr}^{3+},y\text{Ni}^{2+}$ ,  $x = 0.06$ ,  $y = 0.02$ . A photo of the LED device is shown in the inset, with the appearance of the working LED device under visible and NIR light.

consist of three excitation bands at 390, 630, and 1000 nm, corresponding to the transitions  ${}^3A_2 \rightarrow {}^3T_1$  ( ${}^3P$ ),  ${}^3A_2 \rightarrow {}^3T_1$  ( ${}^3F$ ), and  ${}^3A_2 \rightarrow {}^3T_2$  ( ${}^3F$ ), respectively, for octahedrally coordinated  $\text{Ni}^{2+}$  ions,<sup>41,42</sup> where no excitation peaks match the energy of our excitation at 460 nm in the PLE spectrum of  $\text{Ni}^{2+}$ . Figure 3a shows the PLE of  $\text{Ni}^{2+}$  along with the PL of low and high  $\text{Cr}^{3+}$  concentration samples, where blue shading indicates the R-band, green shading the N-band, and orange shading the C-band. The R- and N-bands correspond to the  ${}^3A_2 \rightarrow {}^3T_1$  ( ${}^3F$ ) transition of  $\text{Ni}^{2+}$ , while the C-band corresponds to the  ${}^3A_2 \rightarrow {}^3T_2$  ( ${}^3F$ ) transition of  $\text{Ni}^{2+}$ , indicating possible energy transfer between the activators.

The proposed energy transfer mechanism is shown in Figure 3b. The energy levels of  $\text{Ni}^{2+}$  in an octahedral environment are fixed centrally, with those of single  $\text{Cr}^{3+}$  on the left and pair/cluster  $\text{Cr}^{3+}$  on the right. Upon 460 nm blue light excitation, single  $\text{Cr}^{3+}$  can be excited to the  ${}^4T_1$  state, where electrons nonradiatively relax to the lowest excited state  ${}^2E$  before emitting 708 nm light (R-band). Simultaneously, energy is transferred to  $\text{Ni}^{2+}$  at the  ${}^3T_1$  energy level, also followed by a nonradiative transition to the lowest excited state,  ${}^3T_2$ , before producing 1250 nm NIR-II light.  $\text{Cr}^{3+}$ – $\text{Cr}^{3+}$  pairs and  $\text{Cr}^{3+}$  clusters can also be excited by 460 nm blue light, resulting in 750 nm (N-band) and 850 nm (C-band) emission, distributing to  $\text{Ni}^{2+}{}^3T_1$  and  ${}^3T_2$  energy levels, respectively. Since energy transfer from  $\text{Cr}^{3+}$  clusters to the  ${}^3T_2$  energy level of  $\text{Ni}^{2+}$  occurs directly and does not require nonradiative transition before emitting NIR-II light, it is reasonable that such a transfer process would be highly efficient.

The efficiencies are calculated for the series through the eq 1 below:

$$\eta_T = 1 - \frac{I_S}{I_0} \quad (1)$$

where  $I_0$  and  $I_S$  are the  $\text{Cr}^{3+}$  emission intensities in the absence and presence of  $\text{Ni}^{2+}$ , respectively,<sup>16</sup> obtained from Tables S5–S8. Since several luminescent centers participated in the energy transfer process ( $\text{Cr}^{3+}$  ions,  $\text{Cr}^{3+}$ – $\text{Cr}^{3+}$  pairs, and  $\text{Cr}^{3+}$  clusters), multiple decay pathways were present. Therefore, it is unreliable to calculate the energy efficiency solely by the decay curve since decay times are observed as average decay times and do not represent any individual luminescent centers. The energy transfer efficiency is found to increase with the concentration of  $\text{Ni}^{2+}$  for both series, with the values of  $x = 0.06$  being higher throughout, reaching a maximum of 93.6 and

98.0% for samples  $x = 0.02$ ,  $y = 0.04$ , and  $x = 0.06$ ,  $y = 0.04$ , respectively, as shown in Figure S12a. Such high energy transfer efficiency can be attributed to the interactions of  $\text{Cr}^{3+}$ – $\text{Ni}^{2+}$  pairs detected through EPR. Therefore, along with the IQE findings, we suggest that it is more effective for  $\text{Cr}^{3+}$  clusters to transfer their energy to the  $\text{Ni}^{2+}$  luminescent center than single  $\text{Cr}^{3+}$  ions. As expected, the energy transfer efficiency increases with sintering temperature due to the higher IQE, shown in Figure S12b, resulting in a maximum of 98.3% at 1550 °C. However, the trend of IQE does not match that of the energy transfer efficiency for the  $x = 0.02$ ,  $y = 0.005$ – $0.04$  and  $x = 0.06$ ,  $y = 0.005$ – $0.04$  series at a sintering temperature of 1250 °C, possibly attributable to concentration quenching and energy loss in the nonradiative relaxation process in the  $\text{Ni}^{2+}$  system.

Energy transfer and concentration quenching are also supported by the decay profiles shown in Figures S13 and S14. The detailed calculation of the decay profiles is elaborated in the Supporting Information. The calculated decay time for  $\text{Cr}^{3+}$  is much shorter for samples with  $x = 0.06$  (0.5 ms for  $y = 0$ ) compared to samples with  $x = 0.02$  (4.3 ms for  $y = 0$ ). The decay time also decreases with increasing the  $y$  for both series, from 4.3 to 2.8 ms for samples with  $x = 0.02$  and from 0.5 to 0.29 ms for samples with  $x = 0.06$ . With the decay profiles of  $\text{Cr}^{3+}$  emission being multiexponential for all samples and shortening with increasing  $y$ , this supports the above-mentioned energy transfer mechanism. It is shown that the line and broadband emissions arise from the two different luminescence sites, from single  $\text{Cr}^{3+}$  and from interacting  $\text{Cr}^{3+}$ , and shortening of the decay time may arise from energy transfer between the two luminescence sites. Alternatively, concentration quenching may also contribute to the reduced decay time.

**Thermal and Pressure Studies.** The temperature-dependent studies are elaborated in the Supporting Information. Both samples show stable emission intensity up to 250 K followed by an obvious decrease, with 47.5% and 44.5% remaining intensity at the 423 K LED device working temperature for  $x = 0.02$ ,  $y = 0.03$ , and  $x = 0.06$ ,  $y = 0.02$ , respectively, indicating slightly better thermal stability for the  $x = 0.02$ ,  $y = 0.03$  sample. The reason for this is that  $\text{Cr}^{3+}$  clusters encompass poorer thermal stability; therefore, the intensity drops slightly more significantly for  $\text{Cr}^{3+}$  cluster-induced NIR-II phosphors at rising temperatures.



The pressure-dependent PL spectra of  $\text{Ni}^{2+}$  emission up to 22.5 GPa for sample  $x = 0.02$ ,  $y = 0.03$  are shown in Figure 3c. The reason for demonstrating the  $x = 0.02$ ,  $y = 0.03$  sample rather than the  $x = 0.06$ ,  $y = 0.02$  sample is because the emission spectrum of  $\text{Cr}^{3+}$  clusters overlaps the monitored  $\text{Ni}^{2+}$  emission spectrum. Henceforth, sample  $x = 0.02$ , and  $y = 0.03$  would be a better candidate for investigating the emission performance to pressure. The shape of the spectrum in Figure 3c remains unchanged as the applied pressure increases, but there is a noticeable shift in position toward higher energies. By applying pressure to the samples, the strength of the crystal field increases, resulting in a shift of the  ${}^3T_2$  level toward higher energy. A pressure-induced shift of  $1268\text{ cm}^{-1}$  is found from ambient pressure to 22.5 GPa, with the peak position changing from 1272 to 1050 nm. The band position is plotted with applied pressure in Figure 3d, where the shift is linearly correlated with the pressure at  $64 \pm 2\text{ cm}^{-1}/\text{GPa}$ . Though the significance of pressure change in LED performance is relatively low, such linearity is helpful in future NIR pressure sensing applications.

**LED Performance.** Sample of  $\text{Mg}_{1-y}\text{Ga}_{2-x}\text{O}_4:x\text{Cr}^{3+},y\text{Ni}^{2+}$ ,  $x = 0.06$ ,  $y = 0.02$  was used to fabricate a 2835 NIR phosphor-converted (pc) light emitting diode (LED) by coating the phosphors onto a blue LED chip with an emission wavelength of 452 nm as a light source. The emission spectrum, radiant flux, and blue light conversion efficiency are listed in Figure 4. The resulting emission from  $\text{Ni}^{2+}$  powered by the blue LED chip ranges over 1000–1600 nm in the NIR-II region, peaking at 1265 nm, with a maximum radiant flux of 23.81 mW at 200 mA driving current. The blue light conversion efficiency decreased over a higher current, leaving 11.9% at a 200 mA driving current. The device is shown in the inset of Figure 4b, and the outstanding luminescent performance results reveal this phosphor series possesses great potential for future applications.

## CONCLUSIONS

In summary, our study on the energy transfer mechanism of the intermediate spinel  $\text{MgGa}_2\text{O}_4$  crystal codoped with  $\text{Cr}^{3+}$  and  $\text{Ni}^{2+}$  has shed light on the potential for achieving near-unity quantum efficient NIR-II emission for pc-LEDs. Diffraction analyses confirm the crystal structures of the synthesized samples and the substitution of  $\text{Cr}^{3+}$  for  $\text{Ga}^{3+}$  at octahedral M1 sites. EPR studies reveal the presence of  $\text{Cr}^{3+}$  clusters, the successful substitution of  $\text{Ni}^{2+}$  for octahedral  $\text{Mg}^{2+}$ , and a strong  $\text{Cr}^{3+}$ – $\text{Ni}^{2+}$  pair interaction. PL measurements demonstrate emission from both luminescent centers, and an energy transfer mechanism is proposed that involves energy transfer from  $\text{Cr}^{3+}$  and  $\text{Cr}^{3+}$  clusters to  $\text{Ni}^{2+}$ . Further, the sintering temperature can be used to tune and enhance the  $\text{Ni}^{2+}$  emission intensity, resulting in an unprecedented NIR-II emission IQE of 97.4%. The insights gained from this study contribute to a deeper understanding of energy transfer mechanisms involving  $\text{Cr}^{3+}$  clusters, opening new possibilities for developing highly efficient and high-performance LEDs operating in the NIR-II window.

## EXPERIMENTAL SECTION

**Reagents.** Gallium oxide ( $\text{Ga}_2\text{O}_3$ , 99.9%) was purchased from Gredmann; magnesium oxide ( $\text{MgO}$ , 99.9%) and chromium oxide ( $\text{Cr}_2\text{O}_3$ , 99.9%) were purchased from Merck; nickel oxide ( $\text{NiO}$ , 97%) was purchased from Acros.

**Synthesis of  $\text{Mg}_{1-y}\text{Ga}_{2-x}\text{O}_4:x\text{Cr}^{3+},y\text{Ni}^{2+}$  ( $x = 0.02/0.06$ ,  $y = 0.005$ – $0.04$ ).** The material was synthesized by using a solid-state reaction method. The precursors were weighed according to stoichiometric ratios and ground in an agate mortar for 20 min. The mixed powders were transferred into an alumina crucible and sintered at 1250 to 1550 °C for 5 h in the air. Finally, the sintered powders were ground in an agate mortar and pestle again. Further characterization and experimental measurements are provided in the Supporting Information.

## ASSOCIATED CONTENT

### Supporting Information

The Supporting Information is available free of charge at <https://pubs.acs.org/doi/10.1021/acs.chemmater.4c00438>.

Details of characterization, Rietveld fit profiles along with refined structural parameters, electron paramagnetic resonance profiles, pressure-dependent decay profiles and calculated decay time, temperature-dependent emission spectra, and decay profiles (PDF)

## AUTHOR INFORMATION

### Corresponding Authors

**Sebastian Mahlik** – Institute of Experimental Physics, Faculty of Mathematics, Physics, and Informatics, University of Gdansk, Gdańsk 80-308, Poland; [orcid.org/0000-0002-9514-049X](https://orcid.org/0000-0002-9514-049X); Email: [sebastian.mahlik@ug.edu.pl](mailto:sebastian.mahlik@ug.edu.pl)

**Grzegorz Leniec** – Department of Nanomaterials Physicochemistry, Faculty of Chemical Technology and Engineering, West Pomeranian University of Technology in Szczecin, Szczecin 70-311, Poland; Email: [Grzegorz.Leniec@zut.edu.pl](mailto:Grzegorz.Leniec@zut.edu.pl)

**Ru-Shi Liu** – Department of Chemistry, National Taiwan University, Taipei 106, Taiwan; [orcid.org/0000-0002-1291-9052](https://orcid.org/0000-0002-1291-9052); Email: [rslu@ntu.edu.tw](mailto:rslu@ntu.edu.tw)

### Authors

**Chih-Yu Chang** – Department of Chemistry, National Taiwan University, Taipei 106, Taiwan

**Ming-Hsuan Huang** – Department of Chemistry, National Taiwan University, Taipei 106, Taiwan

**Kuan-Chun Chen** – Department of Chemistry, National Taiwan University, Taipei 106, Taiwan

**Wen-Tse Huang** – Department of Chemistry, National Taiwan University, Taipei 106, Taiwan

**Mikołaj Kamiński** – Institute of Experimental Physics, Faculty of Mathematics, Physics, and Informatics, University of Gdansk, Gdańsk 80-308, Poland

**Natalia Majewska** – Institute of Experimental Physics, Faculty of Mathematics, Physics, and Informatics, University of Gdansk, Gdańsk 80-308, Poland; [orcid.org/0000-0002-1933-0355](https://orcid.org/0000-0002-1933-0355)

**Tomasz Klimczuk** – Faculty of Applied Physics and Mathematics and Advanced Materials Centre, Gdansk University of Technology, Gdańsk 80-233, Poland; [orcid.org/0000-0002-7089-4631](https://orcid.org/0000-0002-7089-4631)

**Jia-Hao Chen** – Everlight Electronics Co., Ltd., New Taipei City 238, Taiwan

**Ding-Hua Cherng** – Everlight Electronics Co., Ltd., New Taipei City 238, Taiwan

**Kuang-Mao Lu** – Everlight Electronics Co., Ltd., New Taipei City 238, Taiwan

**Wei Kong Pang** – Institute for Superconducting and Electronic Materials, University of Wollongong, North Wollongong, New

South Wales 2500, Australia; [orcid.org/0000-0002-5118-3885](https://orcid.org/0000-0002-5118-3885)

**Vanessa K. Peterson** – Institute for Superconducting and Electronic Materials, University of Wollongong, North Wollongong, New South Wales 2500, Australia; Australian Centre for Neutron Scattering, Australian Nuclear Science and Technology Organisation, Sydney, New South Wales 2232, Australia

Complete contact information is available at:  
<https://pubs.acs.org/10.1021/acs.chemmater.4c00438>

### Author Contributions

The manuscript was written with contributions from all authors. All authors have given approval to the final version of the manuscript.

### Notes

The authors declare no competing financial interest.

### ACKNOWLEDGMENTS

This work was financially supported by the Ministry of Science and Technology in Taiwan (contract nos. NSTC 112-2113-M-002-020 and NSTC 113-2923-M-002-006), the National Science Center Poland Grant Opus No. 2018/31/B/ST4/00924, and the National Centre for Research and Development Poland Grant No. PL-TW/VIII/1/2021. NPD data on Echidna were collected under proposal MI13201.

### REFERENCES

- (1) Antaris, A. L.; Chen, H.; Cheng, K.; Sun, Y.; Hong, G.; Qu, C.; Diao, S.; Deng, Z.; Hu, X.; Zhang, B.; Zhang, X.; Yaghi, O. K.; Alamparambil, Z. R.; Hong, X.; Cheng, Z.; Dai, H. A Small-Molecule Dye for NIR-II Imaging. *Nat. Mater.* **2016**, *15*, 235–242.
- (2) Chen, Y.; Xue, L.; Zhu, Q.; Feng, Y.; Wu, M. Recent Advances in Second Near-Infrared Region (NIR-II) Fluorophores and Biomedical Applications. *Front. Chem.* **2021**, *9*, No. 750404.
- (3) Shi, T.; Huang, C.; Li, Y.; Huang, F.; Yin, S. NIR-II Phototherapy Agents with Aggregation-Induced Emission Characteristics for Tumor Imaging and Therapy. *Biomater.* **2022**, *285*, No. 121535.
- (4) An, D.; Fu, J.; Zhang, B.; Xie, N.; Nie, G.; Ågren, H.; Qiu, M.; Zhang, H. NIR-II Responsive Inorganic 2D Nanomaterials for Cancer Photothermal Therapy: Recent Advances and Future Challenges. *Adv. Funct. Mater.* **2021**, *31*, 2101625.
- (5) Liu, B. M.; Guo, X. X.; Huang, L.; Zhou, R. F.; Zou, R.; Ma, C. G.; Wang, J. A Super-Broadband NIR Dual-Emitting  $\text{Mg}_2\text{SnO}_4:\text{Cr}^{3+},\text{Ni}^{2+}$  Phosphor for Ratiometric Phosphor-Converted NIR Light Source Applications. *Adv. Mater. Technol.* **2023**, *8*, 2201181.
- (6) Nair, G. B.; Swart, H.; Dhoble, S. A Review on the Advancements in Phosphor-Converted Light Emitting Diodes (pc-LEDs): Phosphor Synthesis, Device Fabrication and Characterization. *Prog. Mater. Sci.* **2020**, *109*, No. 100622.
- (7) Zhao, F.; Song, Z.; Liu, Q. Advances in Chromium-Activated Phosphors for Near-Infrared Light Sources. *Laser Photonics Rev.* **2022**, *16*, 2200380.
- (8) Chang, C. Y.; Majewska, N.; Chen, K. C.; Huang, W. T.; Lesniewski, T.; Leniec, G.; Kaczmarek, S. M.; Pang, W. K.; Peterson, V. K.; Cherng, D. H.; Lu, K. M.; Mahlik, S.; Liu, R. S. Broadening Phosphor-Converted Light-Emitting Diode Emission: Controlling Disorder. *Chem. Mater.* **2022**, *34*, 10190–10199.
- (9) Cai, H.; Liu, S.; Song, Z.; Liu, Q. Tuning Luminescence from NIR-I to NIR-II in  $\text{Cr}^{3+}$ -Doped Olivine Phosphors for Nondestructive Analysis. *J. Mater. Chem. C* **2021**, *9*, 5469–5477.
- (10) Yuan, L.; Jin, Y.; Wu, H.; Deng, K.; Qu, B.; Chen, L.; Hu, Y.; Liu, R. S.  $\text{Ni}^{2+}$ -Doped Garnet Solid-Solution Phosphor-Converted Broadband Shortwave Infrared Light-Emitting Diodes toward Spectroscopy Application. *ACS Appl. Mater. Interfaces* **2022**, *14*, 4265–4275.
- (11) Yang, Z.; Zhao, Y.; Zhou, Y.; Qiao, J.; Chuang, Y. C.; Molokeev, M. S.; Xia, Z. Giant Red-Shifted Emission in  $(\text{Sr},\text{Ba})\text{-Y}_2\text{O}_4:\text{Eu}^{2+}$  Phosphor Toward Broadband Near-Infrared Luminescence. *Adv. Funct. Mater.* **2022**, *32*, 2103927.
- (12) Kumar, G. A.; Pokhrel, M.; Martinez, A.; Dennis, R. C.; Villegas, I. L.; Sardar, D. K. Synthesis and Spectroscopy of Color Tunable  $\text{Y}_2\text{O}_3:\text{Yb}^{3+},\text{Er}^{3+}$  Phosphors with Intense Emission. *J. Alloys Compd.* **2012**, *513*, 559–565.
- (13) Liu, B. M.; Gu, S. M.; Huang, L.; Zhou, R. F.; Zhou, Z.; Ma, C. G.; Zou, R.; Wang, J. Ultra-Broadband and High-Efficiency Phosphors to Brighten NIR-II Light Source Applications. *Cell Rep. Phys. Sci.* **2022**, *3*, No. 101078.
- (14) Zhou, S.; Feng, G.; Wu, B.; Jiang, N.; Xu, S.; Qiu, J. Intense Infrared Luminescence in Transparent Glass-Ceramics containing  $\beta\text{-Ga}_2\text{O}_3:\text{Ni}^{2+}$  Nanocrystals. *J. Phys. Chem. C* **2007**, *111*, 7335–7338.
- (15) Gao, Y.; Wang, B.; Liu, L.; Shinozaki, K. Near-Infrared Engineering for Broad-Band Wavelength-Tunable in Biological Window of NIR-II and-III: A Solid Solution Phosphor of  $\text{Sr}_{1-x}\text{Ca}_x\text{TiO}_3:\text{Ni}^{2+}$ . *J. Lumin.* **2021**, *238*, No. 118235.
- (16) Wang, C.; Zhang, Y.; Han, X.; Hu, D.; He, D.; Wang, X.; Jiao, H. Energy Transfer Enhanced Broadband Near-Infrared Phosphors:  $\text{Cr}^{3+}/\text{Ni}^{2+}$  Activated  $\text{ZnGa}_2\text{O}_4\text{-Zn}_2\text{SnO}_4$  Solid Solutions for the Second NIR Window Imaging. *J. Mater. Chem. C* **2021**, *9*, 4583–4590.
- (17) Miao, S.; Liang, Y.; Zhang, Y.; Chen, D.; Wang, X. J. Blue LED-Pumped Broadband Short-Wave Infrared Emitter Based on  $\text{LiMgPO}_4:\text{Cr}^{3+},\text{Ni}^{2+}$  Phosphor. *Adv. Mater. Technol.* **2022**, *7*, 2200320.
- (18) Liu, B. M.; Guo, X. X.; Cao, L. Y.; Huang, L.; Zou, R.; Zhou, Z.; Wang, J. A High-Efficiency Blue-LED-Excitable NIR-II-Emitting  $\text{MgO}:\text{Cr}^{3+},\text{Ni}^{2+}$  Phosphor for Future Broadband Light Source toward Multifunctional NIR Spectroscopy Applications. *J. Chem. Eng.* **2023**, *452*, No. 139313.
- (19) Tsai, Y. T.; Huang, Y. K.; Jiang, Z. F.; Yao, Y.; Lo, P. H.; Chao, Y. C.; Lin, B. H.; Lin, C. C. Cation Substitution-Induced Partial Inversion to Pervade Short-Wave Infrared Light for Improving the Accuracy of Artificial Intelligence Image Recognition System. *ACS Materials Lett.* **2023**, *5*, 738–743.
- (20) Zhang, Q.; Liu, D.; Wang, Z.; Dang, P.; Lian, H.; Li, G.; Lin, J.  $\text{LaMgGa}_{11}\text{O}_{19}:\text{Cr}^{3+},\text{Ni}^{2+}$  as Blue-Light Excitable Near-Infrared Luminescent Materials with Ultra-Wide Emission and High External Quantum Efficiency. *Adv. Opt. Mater.* **2023**, *11*, 2202478.
- (21) Miao, S.; Liang, Y.; Shi, R.; Wang, W.; Li, Y.; Wang, X. J. Broadband Short-Wave Infrared-Emitting  $\text{MgGa}_2\text{O}_4:\text{Cr}^{3+},\text{Ni}^{2+}$  Phosphor with Near-Unity Internal Quantum Efficiency and High Thermal Stability for Light-Emitting Diode Applications. *ACS Appl. Mater. Interfaces* **2023**, *15*, 32580–32588.
- (22) Yao, L.; Jia, Q.; Yu, S.; Liang, C.; Jiang, J.; Shao, Q. Simultaneous Absorption and Near-Infrared Emission Enhancement of  $\text{Cr}^{3+}$  Ions in  $\text{MgGa}_2\text{O}_4$  Spinel Oxide via Anionic F-Substitution. *Adv. Opt. Mater.* **2023**, *11*, 2202458.
- (23) Rajendran, V.; Chang, C. Y.; Huang, M. H.; Chen, K. C.; Huang, W. T.; Kamiński, M.; Lesniewski, T.; Mahlik, S.; Leniec, G.; Lu, K. M.; Wei, D. H.; Chang, H.; Liu, R. S. Chromium Cluster Luminescence: Advancing Near-Infrared Light-Emitting Diode Design for Next-Generation Broadband Compact Light Sources. *Adv. Opt. Mater.* **2023**, 2302645.
- (24) Henderson, B.; Imbusch, G. F. *Optical Spectroscopy of Inorganic Solids*, Vol. 44. Oxford University Press, 2006.
- (25) Yuan, L.; Jin, Y.; Zhu, D.; Mou, Z.; Xie, G.; Hu, Y.  $\text{Ni}^{2+}$ -Doped Yttrium Aluminum Gallium Garnet Phosphors: Bandgap Engineering for Broad-Band Wavelength-Tunable Shortwave-Infrared Long-Persistent Luminescence and Photochromism. *ACS Sustain. Chem. Eng.* **2020**, *8*, 6543–6550.
- (26) Toby, B. H. R Factors in Rietveld Analysis: How Good is Good Enough? *Powder Diffr.* **2006**, *21*, 67–70.

- (27) Shannon, R. D. Revised Effective Ionic Radii and Systematic Studies of Interatomic Distances in Halides and Chalcogenides. *Acta Cryst. A* **1976**, *32*, 751–767.
- (28) Schwarz, L.; Galazka, Z.; Gesing, T. M.; Klimm, D. On the Influence of Inversion on Thermal Properties of Magnesium Gallium Spinel: Dedicated to the 80th Birthday of Prof. Joachim Bohm. *Cryst. Res. Technol.* **2015**, *50*, 961–966.
- (29) Koningsberger, D. C.; Prins, R. *X-Ray Absorption: Principles, Applications, Techniques of EXAFS, SEXAFS and XANES*: United States, 1987.
- (30) Yamamoto, T. Assignment of Pre-Edge Peaks in K-edge X-Ray Absorption Spectra of 3d Transition Metal Compounds: Electric Dipole or Quadrupole? *X-Ray Spectrometry: An International Journal* **2008**, *37*, 572–584.
- (31) Leniec, G. Electron Paramagnetic Resonance: A Technique to Locate the Nearest Environment of Chromium Luminescent Centers. *ACS Appl. Opt. Mater.* **2023**, *1*, 1114–1121.
- (32) Rajendran, V.; Fang, M. H.; Huang, W. T.; Majewska, N.; Lesniewski, T.; Mahlik, S.; Leniec, G.; Kaczmarek, S. M.; Pang, W. K.; Peterson, V. K.; Lu, K. M.; Chang, H.; Liu, R. S. Chromium Ion Pair Luminescence: A Strategy in Broadband Near-Infrared Light-Emitting Diode Design. *J. Am. Chem. Soc.* **2021**, *143*, 19058–19066.
- (33) Bobrowska, M.; Typek, J.; Leniec, G.; Zolnierkiewicz, G.; Filipek, E.; Prokop, A.; Blonska-Tabero, A. A Novel Look at Magnetism in Ni<sub>2</sub>FeVO<sub>6</sub>. *IEEE Trans. Magn.* **2022**, *58*, 1–10.
- (34) Worsztynowicz, A.; Kaczmarek, S. M.; Bosacka, M.; Mody, V.; Czernuszewicz, R. S. Structural and Magnetic Characterization of the Cr<sup>3+</sup> and Ni<sup>2+</sup> Ion Species in Ni<sub>2</sub>CrV<sub>3</sub>O<sub>11</sub>. *Rev. Adv. Mater. Sci.* **2007**, *14*, 24–32.
- (35) Tomono, Y.; Kato, T.; Tanokura, Y. EPR Spectra from Ni<sup>2+</sup> Pairs in KZnF<sub>3</sub> Crystals. *J. Phys. Soc. Jpn.* **1984**, *53*, 773–779.
- (36) Bleaney, B. Anomalous Paramagnetism of Copper Acetate. *Rev. Mod. Phys.* **1953**, *25*, 161.
- (37) Ellis, R. S. *Entropy, Large Deviations, and Statistical Mechanics*, Vol. 1431. Taylor & Francis, 2006.
- (38) Sayler, R. I.; Hunter, B. M.; Fu, W.; Gray, H. B.; Britt, R. D. EPR Spectroscopy of Iron-and Nickel-Doped [ZnAl]-Layered Double Hydroxides: Modeling Active Sites in Heterogeneous Water Oxidation Catalysts. *J. Am. Chem. Soc.* **2020**, *142*, 1838–1845.
- (39) Rajendran, V.; Chen, K. C.; Huang, W. T.; Kamiński, M.; Grzegorzcyk, M.; Mahlik, S.; Leniec, G.; Lu, K. M.; Wei, D. H.; Chang, H.; Liu, R. S. Unraveling Luminescent Energy Transfer Pathways: Futuristic Approach of Miniature Shortwave Infrared Light-Emitting Diode Design. *ACS Energy Lett.* **2023**, *8*, 2395–2400.
- (40) Suzuki, T.; Murugan, G. S.; Ohishi, Y. Spectroscopic Properties of a Novel Near-Infrared Tunable Laser Material Ni:MgGa<sub>2</sub>O<sub>4</sub>. *J. Lumin.* **2005**, *113*, 265–270.
- (41) Pappalardo, R.; Wood, D. L.; Linares, R. C., Jr Optical Absorption Spectra of Ni-Doped Oxide Systems. *J. Chem. Phys.* **1961**, *35*, 1460–1478.
- (42) Koetke, J.; Huber, G.; Petermann, K. Spectroscopy of Ni<sup>2+</sup>-Doped Garnets and Perovskites for Solid State Lasers. *J. Lumin.* **1991**, *48*, 564–568.

